Check for updates

Novel perovskite-based composites, La₁₋ₓNdₓFeO₃@activated carbon, as efficient catalysts for the degradation of organic pollutants by heterogeneous electro-Fenton reactions

Qijun Wang,[ab] Shu Zhou,[a] Song Xiao,[a] Feifei Wei,[a] Xuezhu Zhao,[a] Jun'e Qu[ac] and Hairen Wang [ID] *[ac]

Perovskites, which have excellent electrocatalytic properties, are promising for use in heterogeneous catalysis. However, the design and development of green and effective electrocatalysts for environmental water treatment remains an arduous challenge. To overcome such difficulties, we present a facile sol–gel method for the design and preparation of a series of perovskite-activated carbon (AC) composites ($La_{1-x}Nd_xFeO_3$@AC) for the degradation of methyl orange (MO) by heterogeneous electro-Fenton reactions. Furthermore, the as-made $La_{0.6}Nd_{0.4}FeO_3$@AC composite anode had the strongest oxidation ability and stability, with MO wastewater and COD removal rates reaching 99.81% and 96.66% within 10 minutes, respectively. As far as we know, the $La_{1-x}Nd_xFeO_3$@AC composites can be regarded as a series of the most effective catalysts for the degradation of MO to date.

1. Introduction

Perovskite materials have fascinated scientists because of their exceptional physical and chemical properties, such as high temperature stability, high oxygen mobility and high stability of the cation oxidation state.[1–3] As one of the most common perovskite-like oxides and a promising material with an abundance of functionalities, lanthanum *ortho*-ferrite ($LaFeO_3$) has been widely applied in areas like environmental decontamination,[4] multi-ferroic materials,[5] gas sensors,[6] solid oxide fuel cells[7] and photocatalysts.[8] Moreover, $LaFeO_3$ can produce free radicals in the presence of hydrogen peroxide (H_2O_2), such as hydroxyl radicals ($^.OH$), and so can achieve efficient oxidation degradation of organic pollutants.[9,10]

From the composition of perovskite oxide ABO_3, it has been found that the type of A site has great influence on the lattice parameters, cell volume and binding energy (BE) of ABO_3.[11] In addition, when lanthanide *ortho*-ferrite ($LnFeO_3$) is used as a gas sensor material, replacing the ion at the Ln site with other cations will effectively improve the sensing properties of $LnFeO_3$ as its gas sensitive properties are closely related to the BE of the

Ln–O bond.[12] The BE between a metal and oxygen, $\Delta H_{(M-O)}$, is usually estimated using the formula below:[12]

$$\Delta H_{(M-O)} = (H_f - mH_s - nD_0/2)/(CN_m) \qquad (1)$$

Here, H_f is the amount of material, M_mO_n is the formation energy of the oxide, H_S is the sublimation energy of the metal, D_0 is the dissociation energy for O_2 and CN is the coordination number for the metal. The BE of the Ln–O bond is typically less than the absolute value of $\Delta H_{(M-O)}$, leading to the easy disruption of the Ln–O bond. Therefore, the smaller the BE of the Ln–O bond, the more oxygen will be generated by the dissociation process, and the accelerated oxidation process will improve the gas sensing properties of $LnFeO_3$.[12,13] Significantly, the influence of the introduction of rare earth metals (REM) has been reported to authenticate that REM can enhance textural/structural properties, increase the oxygen storage/release capacity (OSC) and can improve the redox behavior of a ceria–zirconia solid solution.[14,15] Interestingly, as one of the REM family, neodymium (Nd) shows its appeal in interatomic interactions. The BEs of Nd–O and La–O bonds are about -136 kJ mol^{-1} and -142 kJ mol^{-1}, respectively.[13] Since the absolute value of the BE of Nd–O is less than that of La–O, it indicates that Nd–O is much easier to dissociate than La–O. We suppose that when La is replaced by Nd, theoretically, the chemisorption of oxygen on the surface of $LaFeO_3$, along with the rate of the oxidation reaction, will increase.

In terms of electrochemistry during the past few decades, electrochemical advanced oxidation processes (EAOPs) have

[a]School of Materials Science and Engineering, Hubei University, Wuhan, 430062, P. R. China. E-mail: whr9999whr@163.com

[b]School of Chemistry & Chemical Engineering, Huazhong University of Science & Technology, Wuhan 430074, P. R. China

[c]Ministry-of-Education Key Laboratory of Green Preparation and Application for Functional Materials, School of Materials Science and Engineering, Hubei University, Wuhan, 430062, P. R. China

drawn scientists' interest in the reclamation of water contaminated with non-biodegradable organics[16–18] because of the capability of EAOPs in generating strong oxidizing radicals that can completely oxidize organic pollutants into CO_2, H_2O and inorganic ions. Electro-Fenton (EF) is the most ubiquitous of these EAOPs, in which the weak oxidant H_2O_2 is continuously generated and supplied to an acidic contaminated solution from the two-electron cathodic reduction of O_2 gas, which proceeds as follows:[19]

$$O_2 + 2H^+ + 2e^- \rightarrow H_2O_2 \qquad (2)$$
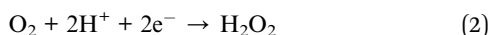
Then, it can be catalytically converted into highly powerful hydroxyl radicals in the presence of an iron catalyst (*e.g.* Fe^{2+} or iron oxides):[20]

$$H_2O_2 + Fe^{2+} \rightarrow Fe^{3+} + {}^{\cdot}OH + OH^- \qquad (3)$$
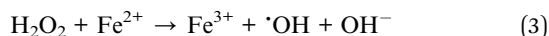
However, the classical EF process has some critical limitations, like the need to operate at pH = 2.0 or 3.0 for an optimum run and the precipitation of soluble iron species used as a catalyst.[17,37] These imperfections could be overcome using an Fe-containing solid catalyst as the source of Fe^{2+} ions instead of soluble iron salt. Hence, it was practically significant to develop a solid heterogeneous catalyst with high activity and stability to deactivation and to metal leaching.

In addition, activated carbon (AC) is a well-known material which is widely used as an admirable adsorbent and supporting material, due to its excellent properties in mechanical strength and porosity.[21]

Therefore, taking into consideration the aforementioned inconveniences of the electro-Fenton system, a strategy is proposed here to prepare a heterogeneous catalyst containing both perovskite oxide and activated carbon (AC). In this study, we prepared $La_{1-x}Nd_xFeO_3$@AC composites *via* a facile sol–gel method. Organic pollutants in wastewater have had a great negative impact on ecological environments, and the latest research has all been devoted to the degradation of organic pollutants.[22,23] Methyl orange (MO), a typical azo dye in textile wastewater, was used as the target pollutant, because azo dye-rich textile wastewater is resistant to conventional biological treatment due to the stability and toxicity of the dye. As an important part of our research system, methyl orange degradation experiments, along with gas chromatography-mass spectrometry (GC-MS) analysis, have been completed precisely to evaluate the electrochemical activities of the $La_{1-x}Nd_xFeO_3$@AC composites.

2. Experimental section

2.1. Materials preparation

All of the chemicals used in this study were of analytical grade and used as received, without further purification. Methyl Orange (MO) (Sinopharm Chemical Reagent Co., Ltd.), which is widely used in the textile industry and as a biological stain, was regarded as the target pollutant. Sodium sulphate (99%, anhydrous) was the supporting electrolyte and iron (III) nitrate

nonahydrate (97%, AR), lanthanum nitrate hydrate (99.9%, AR), neodymium nitrate hexahydrate (99.0%, AR) were used as catalysts. Citric acid (99.5%) was obtained from Tianjin Bodi Chemical Co., Ltd and used as received. Deionized water, obtained with a Milli-Q water purification system (Millipore, France), was used for the preparation of solutions.

2.2. Modification of activated carbon and preparation of $La_{1-x}Nd_xFeO_3$@AC catalysts

2.2.1. Oxidation with nitric acid in liquid phase and functionalization with urea. In a typical treatment, a certain quantity of raw activated carbon was soaked for 24 h in dilute nitric acid to remove impurities, and then the ACs were thoroughly washed with deionized water until neutrality of the scrubbing solution was reached. They were then further dried in an oven for 6 h at 100 °C. The obtained ACs were denoted modified ACs.

2.2.2. Preparation of $La_{1-x}Nd_xFeO_3$@AC catalysts. $La_{1-x}Nd_xFeO_3$@AC was prepared by a sol–gel preparation method. $Fe(NO_3)_3 \cdot 9H_2O$, $La(NO_3)_3 \cdot 2.5H_2O$, $Nd(NO_3)_3 \cdot 6H_2O$ and citric acid ($C_6H_8O_7 \cdot H_2O$) were used as raw materials. The gel precursor was prepared as follows. Modified ACs were added into a mixed aqueous solution of $La(NO_3)_3 \cdot 2.5H_2O$ (La), $Nd(NO_3)_3 \cdot 6H_2O$ (Nd), $Fe(NO_3)_3 \cdot 9H_2O$ (Fe) and citric acid (CA) under vigorous stirring at ambient temperature and at the composition in molar ratio of La/Nd/Fe/CA = $1.0 - x/x/1.0/3.0$ ($x = 0, 0.2, 0.4, 0.6, 0.8, 1$). Subsequently, the solution was stirred for 1 h at 80 °C, and then heated to the boiling point of water (100 °C). The gel precursor was dried in air at 120 °C for 6 h, and then the resulting material was heated from room temperature to 700 °C under an argon atmosphere and calcined at 700 °C for 3 h.

2.2.3. Preparation of the air diffusion cathode. The air diffusion cathode was prepared using the following procedure.[12] After undergoing stirring for 20 s, the mixture of 1.5 mL distilled water, 1.5 mL PTFE (mass fraction 60%) and 0.27 g carbon black was pasted uniformly onto one side of the PAN carbon felt (3×5 cm^2). After it had dried naturally, the coated carbon felt was heated at 350 °C for 30 min. After it had cooled down, a mixture of 5.82 mL distilled water, 0.09 mL PTFE (mass fraction 60%), 0.18 g carbon black and 0.5 mL isopropanol was made and stirred for 20 s. The same procedure was utilized to coat this mixture onto the same side of carbon felt. The first carbon black layer was waterproof and used for electric conduction, while the second layer was for H_2O_2 production.

2.3. Electrochemical system

A cylindrical glass cell (0.5 L and a diameter of 5 cm) was used to carry out the electrochemical experiments. A PAN air diffusion cathode (3 cm × 5 cm) was fitted on the inner side of the cell. An anode basket made from a stainless steel wire mesh full of the $LaFeO_3$@AC catalyst was centered into the cell. The electrolysis solution was prepared by adding sodium sulphate into methyl orange solution. The pH of the solution was set to 2.0 using sulfuric acid solution (1 mol L^{-1}) and a pH meter. After that, the solution was transferred to the electrochemical cell and stirred (500 rpm) with a magnetic stirrer. The oxygen

demand of the system was provided by air bubbling with a compressed air system. The current was controlled with an electrochemical workstation.

Liquid samples were withdrawn periodically for UV-vis spectro-photometer analysis and chemical oxygen demand (COD) measurements. Before each analysis, sample aliquots withdrawn from treated solutions were filtered with 0.45 μm PTFE filters.

All of the investigations were carried out in triplicate to avoid any discrepancy in experimental results and averages were reported. The removal efficiency of phenol could be calculated using the following equation:

$$\text{Removal } (\%) = [C_0 - C_t]/C_0 \times 100\% \tag{4}$$

C_0 and C_t were the initial and final absorbance values at 507 nm of the methyl orange wastewater, or the initial and final COD, respectively.

2.4. Composite $La_{1-x}Nd_xFeO_3$/AC characterization and analytical method

The specific surface areas of the binding catalysts were determined by the nitrogen adsorption method (automated gas adsorption apparatus, Micromeritics Inc. ASAP 2020 HD88), performed at −196 °C. Before the gas adsorption measurement, all of the samples were degassed at 250 °C in a vacuum (10^{-3} torr) for 12 h. Surface areas and the micropore volume of samples were determined using the Brunauer–Emmett–Teller (BET) and Dubinin–Radushkevich (D–R) equations.

The pH at the point of zero charge (pH_{PZC}) was determined by mixing 0.05 g of each sample with 20 mL of 0.01 mol L^{-1} NaCl aqua-solution, with pH values adjusted between 2.0 and 11.0 by adding 0.1 mol L^{-1} HCl or 0.1 mol L^{-1} NaOH aqua-solution. The final pH was measured after 48 h of shaking at room temperature. Blank experiments (without the addition of carbon) were also performed for each pH and the values measured after 48 h are considered as the initial pH, in order to avoid the variation of pH caused by the effect of CO_2 present in the headspace. The pH_{PZC} value of each carbon sample was determined by intercepting the obtained final pH vs. initial pH curve with the straight line final pH = initial pH.[24]

The phases of the binding catalysts were identified by means of X-ray diffraction (XRD), using a Rigaku D/max-IIIC under Cu Kα radiation ($\lambda = 1.5418$ Å), at a scanning range of 2 theta (2θ) = 10–80° and under a speed of 4° per minute. The average crystallite size of the catalysts was estimated using the Debye–Scherrer equation:

$$D = \frac{0.90\lambda}{\beta \cos \theta} \tag{5}$$

where D is the crystallite size (nm), λ is the wavelength (nm), β is the corrected full width at half maximum (radian) and θ is the Bragg angle (radian).

The morphology and size distribution of the metal oxides as well as the elemental analyses of the binding catalysts were examined using a scanning electron microscope (SEM-JEOL

JSM6510LV) equipped with energy dispersive spectrometry (EDS).

X-ray photoelectron spectra (XPS) were recorded at room temperature on a Thermo Fisher Scientific 250Xi analyzer with a magnesium anode under Kα ($h\nu = 1486.6$ eV) radiation. Gas chromatography-mass spectrometry analysis was carried out using an Agilent 6890 GC/5975MSD GC-MS analyzer.

3. Results and discussion

3.1. Characterization of the composite $La_{1-x}Nd_xFeO_3$@AC

3.1.1. X-Ray Diffraction (XRD) characterization. XRD characterization diagrams of modified AC along with $La_{1-x}Nd_xFeO_3$@AC ($x = 0, 0.2, 0.4, 0.6, 0.8$ or 1.0) are shown in Fig. 1. The diffraction peaks can be observed at the position of $2\theta = 22.62°, 32.18°, 39.69°, 46.16°, 52.04°, 57.37°, 67.38°$ and $76.65°$ (Fig. 1a). This corresponds to the characteristic diffraction peaks of orthorhombic $LaFeO_3$ (JCPDS#88-0641).[25]

As is shown in Fig. 1b (after the magnification of 2θ between 31–33° in Fig. 1a), with an enhanced ratio of Nd in $La_{1-x}Nd_xFeO_3$@AC, the diffraction peak at $2\theta = 32.18°$ continues to drift to the right, along with the continuous change for the lattice of $La_{1-x}Nd_xFeO_3$. By Bragg's law,[26] $2d \sin \theta = n\lambda$, an increase in the diffraction angle θ will lead to a decrease in the crystal interplanar spacing d, which simply means that the cell of $La_{1-x}Nd_xFeO_3$@AC has a tendency to shrink gradually with an increase in the doping ratio of Nd. When $x = 1.0$, the diffraction peaks which appear at $22.96°$, $25.64°, 32.31°, 40.37°, 46.50°, 53.33°, 58.54°, 68.33°$ and $77.79°$ (Fig. 1a) correspond to the characteristic diffraction peak of orthorhombic $NdFeO_3$ (JCPDS#25-1149).[27] No characteristic peaks of La_2O_3, Nd_2O_3 and Fe_2O_3 were detected, indicating that the metal nitrates have been completely decomposed to form single phase $La_{1-x}Nd_xFeO_3$ composite oxides. Furthermore, as shown in Table 1, the cell volume (V) and the average grain size tended to be smaller with increases in the proportion of Nd in $La_{1-x}Nd_xFeO_3$@AC, because the radius of Nd^{3+} (0.983) is
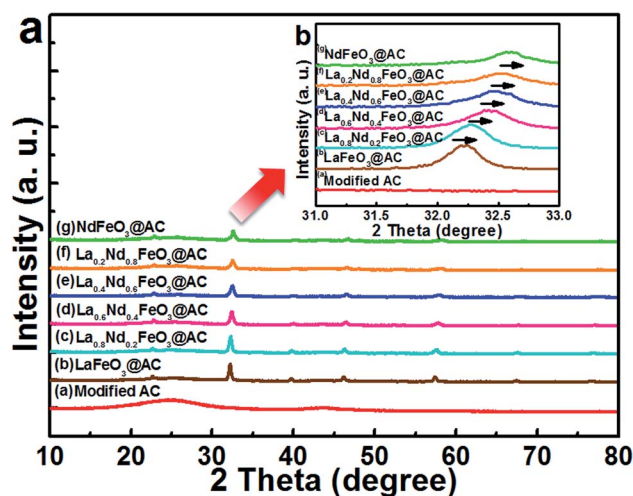
Fig. 1 XRD energy spectra of (a) modified AC; (b) $LaFeO_3$@AC; (c) $La_{0.8}Nd_{0.2}FeO_3$@AC; (d) $La_{0.6}Nd_{0.4}FeO_3$@AC; (e) $La_{0.4}Nd_{0.6}FeO_3$@AC; (f) $La_{0.2}Nd_{0.8}FeO_3$@AC; (g) $NdFeO_3$@AC.

Table 1 The lattice parameters and pH_{PZC} of modified AC and $La_{1-x}Nd_xFeO_3@AC$

Samples	a (Å)	b (Å)	c (Å)	V (Å^3)	$\alpha = \beta = \gamma$ (°)	Average grain size (nm)	pH_{PZC}
Modified AC	—	—	—	—	—	—	2.82
$LaFeO_3@AC$	5.9237	5.7267	7.1342	242.0153	90	309	6.56
$La_{0.8}Nd_{0.2}FeO_3@AC$	5.6241	5.5751	7.6785	240.7594	90	251	6.63
$La_{0.6}Nd_{0.4}FeO_3@AC$	5.5295	5.7329	7.5548	239.4875	90	207	6.90
$La_{0.4}Nd_{0.6}FeO_3@AC$	5.5216	5.5280	7.7742	237.2951	90	189	7.20
$La_{0.2}Nd_{0.8}FeO_3@AC$	5.8160	5.6117	7.2449	236.4567	90	185	7.36
$NdFeO_3@AC$	5.3326	5.5479	7.8760	233.0093	90	210	7.58

slightly smaller than that of La^{3+} (0.114).[28] Therefore, the cell volume of $NdFeO_3@AC$ is the smallest one (233.0093 Å^3) in this series of $La_{1-x}Nd_xFeO_3@AC$ composites.

3.1.2. Scanning electron microscope (SEM) characterization. The surface morphology of modified AC, such as AC and $La_{1-x}Nd_xFeO_3@AC$ (x = 0, 0.2, 0.4, 0.6, 0.8, 1.0), was scanned using SEM, and the results are shown in Fig. 2. As shown in Fig. 2a, the modified AC with dilute nitric acid has a smooth surface and holes on the surface are clearly visible, with no apparent granules or flakes. The SEM images of $La_{1-x}Nd_xFeO_3@AC$ (x = 0, 0.2, 0.4, 0.6, 0.8, 1.0) are shown in Fig. 2b–g. When x = 0, the surface of $LaFeO_3@AC$ is mainly loaded with cubes (or chips) and particles. Nevertheless, when x = 0.2, 0.4, 0.6 or 0.8 (Fig. 1b–f), the load ratio of cubes (or chips) on the surface of $La_{1-x}Nd_xFeO_3@AC$ decreases gradually with increasing proportions of Nd, and the particles gradually increased. Moreover, when x = 1, which simply means that $La_{1-x}Nd_xFeO_3@AC$ changes to $NdFeO_3@AC$, the cubes (or chips) can be observed on the surface again (Fig. 2g).

3.1.3. Energy dispersive spectrometry (EDS) characterization. The results of the surface EDS elemental scanning of modified AC and $La_{1-x}Nd_xFeO_3@AC$ (x = 0, 0.2, 0.4, 0.6, 0.8 or 1.0) are displayed in Table 2 and Fig. 3. The modified AC surface is mainly C and O elements, while the mass fraction is 92.81% and 7.19%, respectively. As shown in Fig. 3b–g, Nd has been successfully incorporated into the lattice of $LaFeO_3@AC$. Table 2 clearly indicates that the maximum mass fraction of O and Fe

in $LaFeO_3@AC$ is 10.81% and 11.68%, respectively. With an increasing Nd ratio in $La_{1-x}Nd_xFeO_3@AC$, the mass fraction of Fe and O decreased, however, the atomic fraction (or amount of material fraction) proportion of (La + Nd) : Fe : O is 1 : 1 : 3, which is much closer to that of the theoretical value.

3.1.4. X-ray photoelectron spectroscopy (XPS) characterization. The full XPS spectra of perovskite catalysts along with the characteristic peaks of C-1s, O-1s, Fe-2p, La-3d and Nd-3d are shown in Fig. 4. The C-1s peak corresponds to the C element in the carrier AC in $La_{1-x}Nd_xFeO_3@AC$, while the peaks of Fe-2p, La-3d and Nd-3d correspond to the Fe, La and Nd elements in the $La_{1-x}Nd_xFeO_3$ oxide of the $La_{1-x}Nd_xFeO_3@AC$ surface, respectively. The content of chemisorbed oxygen and chemically adsorbed water in the O-1s characteristic peaks in $La_{1-x}Nd_xFeO_3@AC$ will be the decisive factor for the oxidative performance of this series of $La_{1-x}Nd_xFeO_3@AC$ composite electrodes.

As shown in Fig. 5, after the O-1s XPS peak deconvolution of $La_{1-x}Nd_xFeO_3@AC$, two peaks can be clearly observed at 529.37–529.64 eV and 531.30–531.47 eV. The former corresponds to lattice oxygen in perovskite oxides (O_α) and the latter belongs to chemically adsorbed oxygen (O_β).[29] The binding energy peaks of chemisorbed H_2O between 532.86–533.07 eV did not appear in Fig. 4a–f, or the peak intensity was quite weak, which coincided with the O-1s XPS energy spectrum of $LaBO_3$ (B=Cu, Fe, Mn, Co, Ni) reported in the literature.[8] As can be
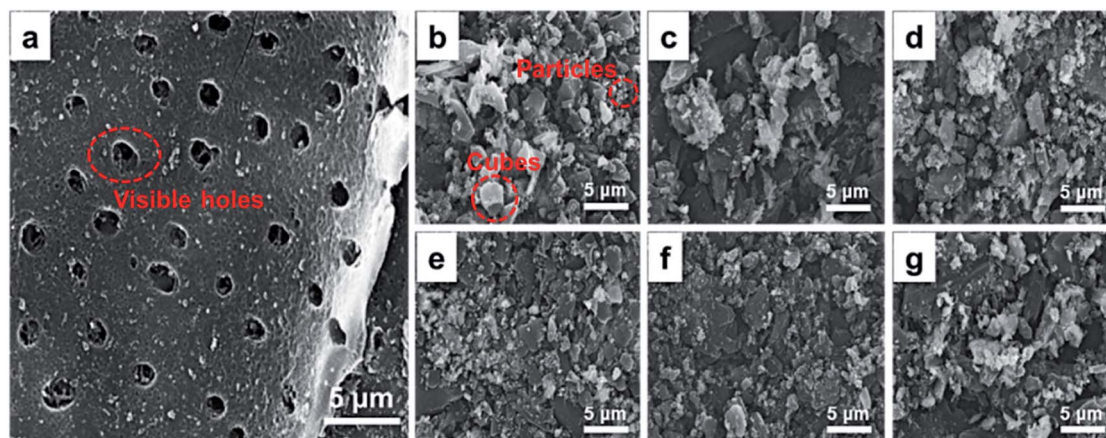
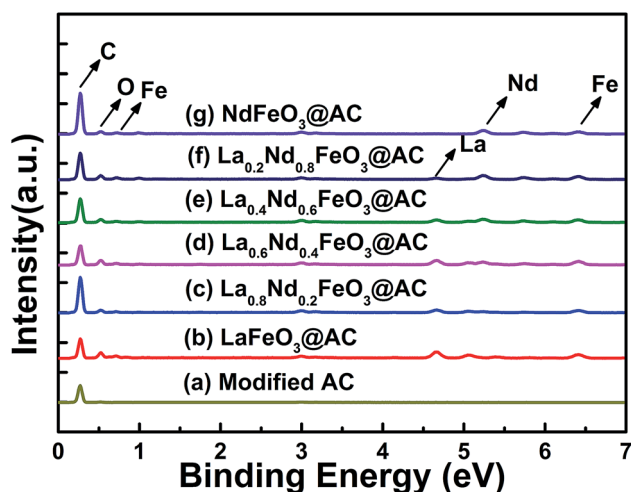**Fig. 2** SEM images of (a) modified AC; (b) $LaFeO_3@AC$; (c) $La_{0.8}Nd_{0.2}FeO_3@AC$; (d) $La_{0.6}Nd_{0.4}FeO_3@AC$; (e) $La_{0.4}Nd_{0.6}FeO_3@AC$; (f) $La_{0.2}Nd_{0.8}FeO_3@AC$; (g) $NdFeO_3@AC$.

Table 2 The elemental content of modified AC and $La_{1-x}Nd_xFeO_3@AC$

Sample	C		O		La		Nd		Fe	
	Wt%	At%	Wt%	At%	Wt%	At%	Wt%	At%	Wt%	At%
Modified AC	92.81	94.50	7.19	5.50	—	—	—	—	—	—
LaFeO₃@AC	51.15	79.85	10.81	12.67	26.36	3.56	—	—	11.68	3.92
La₀.₈Nd₀.₂FeO₃@AC	71.82	90.68	6.12	5.80	10.74	1.17	4.37	0.46	6.69	1.89
La₀.₆Nd₀.₄FeO₃@AC	50.36	81.56	8.66	10.53	17.15	2.40	13.08	1.76	10.75	3.74
La₀.₄Nd₀.₆FeO₃@AC	58.85	86.88	6.50	7.20	9.73	1.24	16.61	2.04	8.31	2.64
La₀.₂Nd₀.₈FeO₃@AC	60.17	86.19	7.73	8.31	4.00	0.50	19.33	2.31	8.76	2.70
NdFeO₃@AC	73.03	91.94	5.08	4.80	—	—	16.07	1.68	5.83	1.58

Fig. 3 EDS of (a) modified AC; (b) LaFeO₃@AC; (c) La₀.₈Nd₀.₂FeO₃@AC; (d) La₀.₆Nd₀.₄FeO₃@AC; (e) La₀.₄Nd₀.₆FeO₃@AC; (f) La₀.₂Nd₀.₈FeO₃@AC; (g) NdFeO₃@AC.
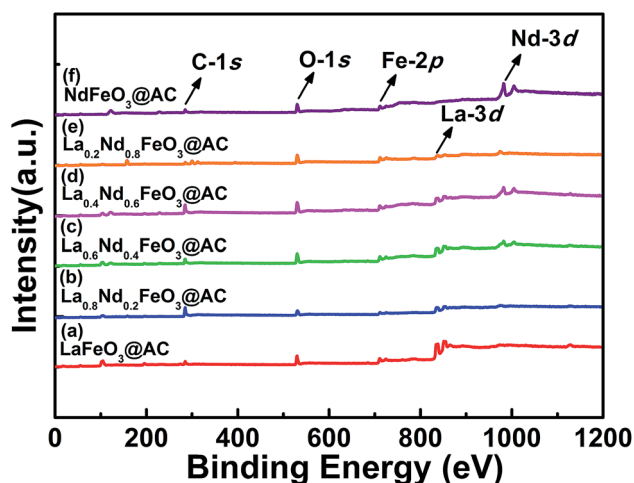
Fig. 4 Survey XPS spectrum of perovskite catalysts: (a) LaFeO₃@AC; (b) La₀.₈Nd₀.₂FeO₃@AC; (c) La₀.₆Nd₀.₄FeO₃@AC; (d) La₀.₄Nd₀.₆FeO₃@AC; (e) La₀.₂Nd₀.₈FeO₃@AC; (f) NdFeO₃@AC.

seen from Table 3, according to the ratio of peak intensity between O_α and O_β, the relative amounts of O_β in LaFeO₃@AC, La₀.₈Nd₀.₂FeO₃@AC, La₀.₆Nd₀.₄FeO₃@AC, La₀.₄Nd₀.₆FeO₃@AC,

La₀.₂Nd₀.₈FeO₃@AC and NdFeO₃@AC (denoted as $O_\beta/(O_\alpha + O_\beta)$) are 24.39%, 48.19%, 64.40%, 57.80%, 40.38% and 39.12%, respectively. Furthermore, the analysis of the XPS peak splitting could be seen to show that the addition of neodymium may induce the formation of ferrous ions, due to the presence of ferrous ions in lanthanum ferrite and oxygen vacancies (or oxygen defects) can be produced while the chemisorbed oxygen content is proportional to the oxygen defect concentration.[30] Therefore, the addition of neodymium greatly increases the catalytic activity of lanthanum ferrite.

To gain an in-depth understanding of the stability and metal leaching of the composite anodes, we further performed an extra XPS contrast measurement of the La₀.₆Nd₀.₄FeO₃@AC composite anode before and after the electrocatalytic oxidation process (Fig. 6).

As can be seen from Fig. 6a, the survey XPS spectrum of the used La₀.₆Nd₀.₄FeO₃@AC composite anode (before and after electrocatalytic oxidation) showed the same characteristic peaks of C-1s, O-1s, Fe-2p, La-3d and Nd-3d. Moreover, Fig. 6b and c show that after O-1s XPS peak deconvolution, four peaks can be clearly observed at 529.29–529.41 eV (lattice oxygen in perovskite oxides) and 531.32–531.40 eV (chemically adsorbed oxygen). This same peak intensity and binding energy clearly indicates that the La₀.₆Nd₀.₄FeO₃@AC composite anode is of perfect stability during the electrocatalytic oxidation process. Particularly, after electrocatalytic oxidation the characteristic peaks of Fe-2p are the same as the original, which can further demonstrate that the interference of the leaching of iron species is negligible.

3.2. Adsorption and electrochemical catalytic oxidation performance of the modified AC and $La_{1-x}Nd_xFeO_3@AC$ composite electrodes

Under conditions without input current, the pH of MO wastewater was adjusted to 2.0 using dilute H₂SO₄ solution, the physical adsorption (Fig. 7a and b) along with electrocatalytic degradation (Fig. 7c and d) performance of the composite anodes was investigated according to the method described above in the experimental section and the removal rates of MO and COD in wastewater were taken as the research index.

As can be seen from Fig. 7a, using modified AC, LaFeO₃@AC, La₀.₈Nd₀.₂FeO₃@AC, La₀.₆Nd₀.₄FeO₃@AC, La₀.₄Nd₀.₆FeO₃@AC, La₀.₂Nd₀.₈FeO₃@AC and NdFeO₃@AC composite electrodes to
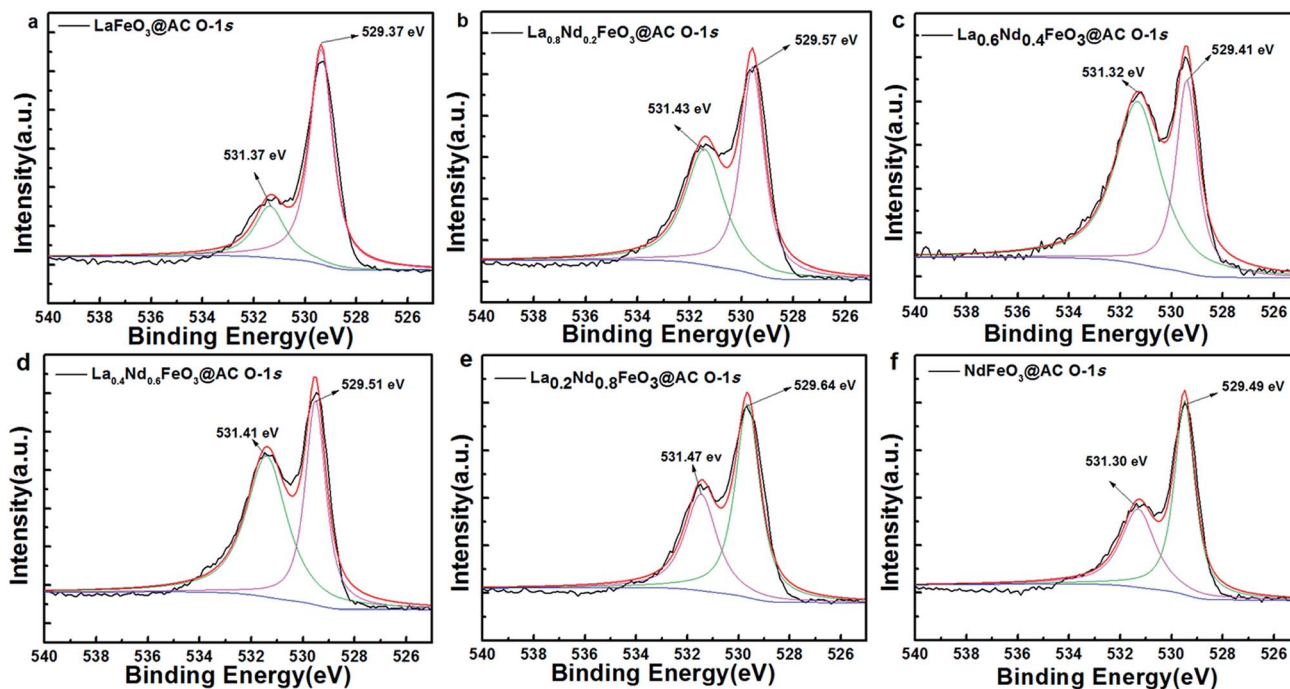
Fig. 5 O-1s XPS patterns of the perovskite catalysts: (a) $LaFeO_3$@AC; (b) $La_{0.8}Nd_{0.2}FeO_3$@AC; (c) $La_{0.6}Nd_{0.4}FeO_3$@AC; (d) $La_{0.4}Nd_{0.6}FeO_3$@AC; (e) $La_{0.2}Nd_{0.8}FeO_3$@AC; (f) $NdFeO_3$@AC.

perform physical adsorption for 10 minutes, the removal rate of MO can reach 11.21%, 12.52%, 14.48%, 15.87%, 16.63%, 17.94% and 18.53%, respectively. Moreover, as shown in Fig. 7b, under the same physical adsorption time, the COD removal rates of these composite electrodes are 33.05%, 34.46%, 34.78%, 35.17%, 35.86%, 36.53% and 37.49%, respectively. The above results show that modified AC, $LaFeO_3$@AC, $La_{0.8}Nd_{0.2}FeO_3$@AC, $La_{0.6}Nd_{0.4}FeO_3$@AC, $La_{0.4}Nd_{0.6}FeO_3$@AC, $La_{0.2}Nd_{0.8}FeO_3$@AC and $NdFeO_3$@AC composite electrodes have a gradually increasing trend in the physical adsorption of MO. In addition, the abilities of the different composite electrodes in the Fe–C primary cell process to remove organic pollutants are very similar to each other,[31] which suggests that the primary cause of differences in MO adsorption capacity between the composite electrodes is the different internal adsorption capacities of AC.

The pH_{PZC} of modified AC, $LaFeO_3$@AC, $La_{0.8}Nd_{0.2}FeO_3$@AC, $La_{0.6}Nd_{0.4}FeO_3$@AC, $La_{0.4}Nd_{0.6}FeO_3$@AC, $La_{0.2}Nd_{0.8}FeO_3$@AC and $NdFeO_3$@AC is 2.82, 6.56, 6.63, 6.90, 7.20, 7.36 and 7.58

respectively (Table 1). According to the theory of pH_{PZC}, if pH < pH_{PZC} (in solution), the surface of the AC will have positive charge.[25] However, when the pH in MO wastewater is 2.0, the surface positive charge in these composite materials can arrange in order and increase gradually, while the positive charge in anionic $C_{14}H_{14}N_3O_3S^-$ in MO gradually increases.[32] Therefore, a larger pH_{PZC} value can lead to more $La_{1-x}Nd_xFeO_3$@AC molecules being adsorbed on MO, along with a higher removal rate of MO and COD.

Under the conditions of pH = 2.0 in MO wastewater and an electrolyte concentration of Na_2SO_4 of 7 g L^{-1}, the composite electrodes were prepared and the electrocatalytic oxidation test

Table 3 O-1s XPS results of the perovskite catalysts

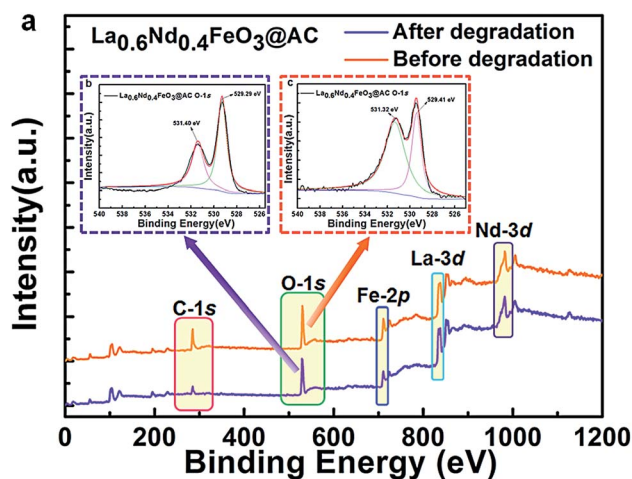| Sample	Binding energy (eV)		
	O_α	O_β	$O_\beta/(O_\alpha + O_\beta)$, %
$LaFeO_3$@AC	529.37	531.37	24.39
$La_{0.8}Nd_{0.2}FeO_3$@AC	529.57	531.43	48.19
$La_{0.6}Nd_{0.4}FeO_3$@AC	529.41	531.32	64.40
$La_{0.4}Nd_{0.6}FeO_3$@AC	529.51	531.41	57.80
$La_{0.2}Nd_{0.8}FeO_3$@AC	529.64	531.47	40.38
$NdFeO_3$@AC	529.49	531.30	39.12

Fig. 6 Survey XPS spectrum and O-1s XPS patterns of the $La_{0.6}Nd_{0.4}FeO_3$@AC composite anode, before and after the electrocatalytic oxidation process.
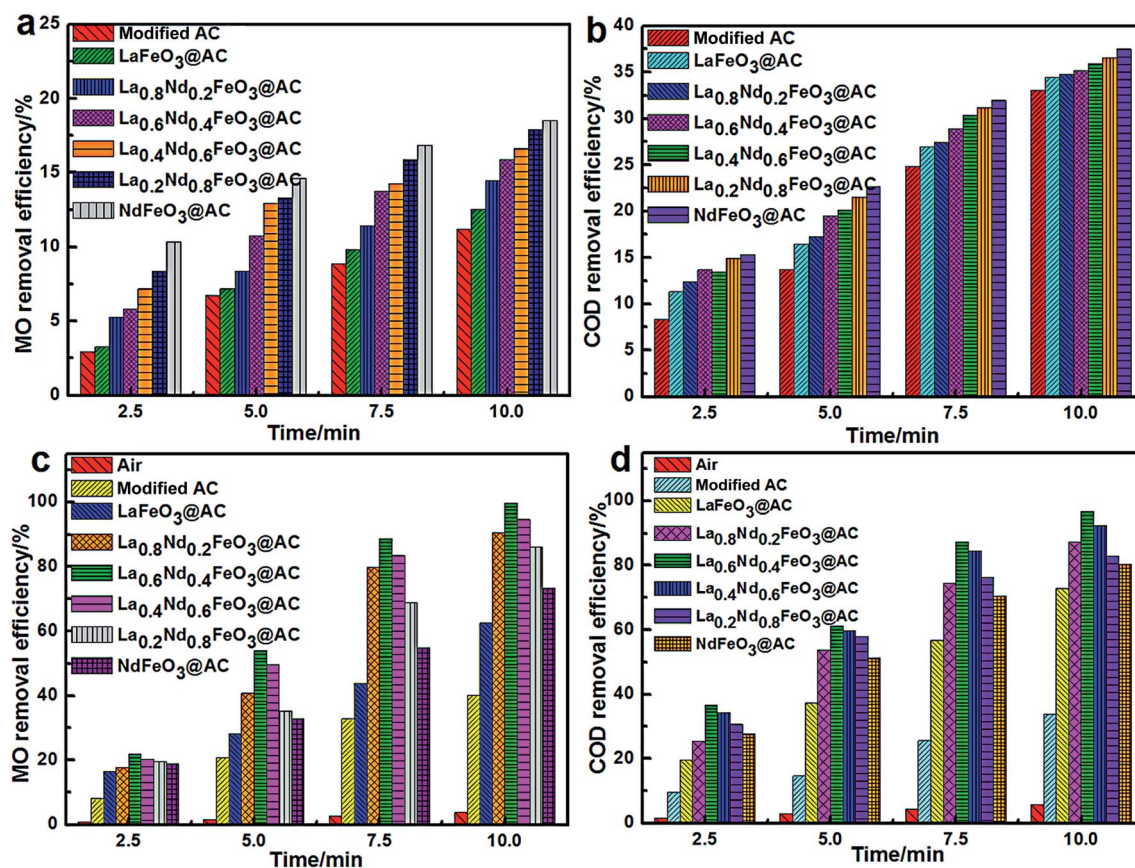
Fig. 7 (a) The MO removal efficiency in MO wastewater of different composite anodes (physical adsorption); (b) the COD removal efficiency in MO wastewater of different composite anodes (physical adsorption); (c) the MO removal efficiency in MO wastewater of different composite anodes and air during the electrocatalytic process; (d) the COD removal efficiency in MO wastewater of different composite anodes and air during the electrocatalytic process.

along with the direct aeration oxidation experiment were carried out. The results are shown in Fig. 7c and d.

Fig. 7c and d show that the removal rates of MO and COD in 10 min were 3.77% and 5.71% when the reaction system was only treated by aeration, which indicates that the air in the MO wastewater oxidation degradation capacity is quite limited.

Furthermore, the removal rates of MO and COD are greatly improved when using the composite electrodes, such as modified AC and $La_{1-x}Nd_xFeO_3$@AC. The modified AC composite electrode is much weaker than the $La_{1-x}Nd_xFeO_3$–AC series of composite electrodes in the resolution reaction of H_2O_2. The electrolytic current density is 400 mA dm^{-2}, and the removal rates of MO and COD in 10 minutes can only reach 40.15% and 33.88%, respectively.

Significantly, the ratio of Nd in $La_{1-x}Nd_xFeO_3$–AC has a great influence on the performance of the composite electrode. When the electrolysis current density is at 400 mA dm^{-2}, in 10 minutes the MO removal rate can reach 62.48%, 90.64%, 99.81%, 94.67%, 86.18% and 73.36% using $LaFeO_3$@AC, $La_{0.8}$-$Nd_{0.2}FeO_3$@AC, $La_{0.6}Nd_{0.4}FeO_3$@AC, $La_{0.4}Nd_{0.6}FeO_3$@AC, $La_{0.2}Nd_{0.8}FeO_3$@AC and $NdFeO_3$@AC composite electrodes. Meanwhile, the removal rates of COD can reach 72.85%, 87.31%, 96.66%, 92.57%, 82.93% and 80.24% in 10 minutes, respectively. In terms of the MO and COD removal rates in MO

wastewater, the $La_{0.6}Nd_{0.4}FeO_3$@AC composite electrode has the strongest activity, and the removal rates of MO and COD can reach 99.81% and 96.66%, respectively, within 10 minutes. In the absence of surface adsorbed H_2O, the highest content of $O_β$ on the surface of $La_{0.6}Nd_{0.4}FeO_3$@AC is 64.40%, leading to the strongest oxidation capacity.[33,34]

Additionally, in order to better understand the MO degradation procedure, color removal properties are investigated and the results are shown in Fig. 8.

It can be clearly seen from Fig. 8 that with the electrocatalysis of $La_{0.6}Nd_{0.4}FeO_3$@AC composite anodes, the decolorization rate of MO can reach 100% within 10 minutes, while the removal rate of COD is as high as 96.66%. These results demonstrate that the chromophore in MO has been basically destroyed, and the organic species are degraded almost completely, which corresponds with the GC-MS analysis.

3.3. Infrared spectrum analysis of MO wastewater before and after reaction

As shown in Fig. 9, the infrared spectra of MO wastewater treated with different composite anodes, such as modified AC and $La_{1-x}Nd_xFeO_3$@AC (x = 0, 0.2, 0.4, 0.6, 0.8 or 1.0), have been obtained in the range of 4000–750 cm^{-1}.
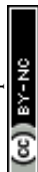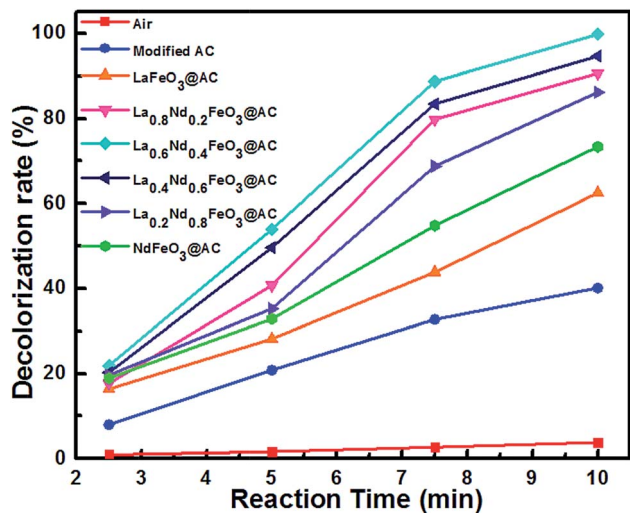
Fig. 8 The decolorization rate of MO wastewater using different composite anodes and air during the electrocatalytic process.

As shown in Fig. 9a, untreated MO wastewater appeared at 1607 cm^{-1} with a double aromatic ring (benzene ring) stretching vibration peak,[35] while in Fig. 9e and f, the transmittance of the stretching vibration peak at 1607 cm^{-1} is almost close to 0, which indicates that the aromatic ring of the MO molecule has been completely destroyed after the MO wastewater was treated using $La_{0.6}Nd_{0.4}FeO_3@AC$ and $La_{0.4}Nd_{0.6}FeO_3@AC$, and the destruction of the aromatic rings in Fig. 9e is more violent than in Fig. 9f.

In Fig. 9f and g, the stretching vibration peaks of aromatic rings can still be observed, indicating that the ability of $La_{1-x}Nd_xFeO_3@AC$ ($x = 0, 0.2, 0.8$ or 1) and modified AC composite anodes to catalyze the oxidation of MO molecules is less than that of $x = 0.4$ and 0.6 in $La_{1-x}Nd_xFeO_3@AC$. As can be seen from Fig. 9b and c, the –N≡N– vibration peak of MO can be observed at 1424 and 1426 cm^{-1} after being treated with a composite anode such as modified AC and $LaFeO_3@AC$.[36] However, as shown in Fig. 9d–h, the vibrational peaks of –N≡N– are already very weak or cannot be observed, and so it can be seen that the composite anodes such as modified AC and $LaFeO_3@AC$ have a weaker decoloration ability for MO wastewater than $La_{1-x}Nd_xFeO_3@AC$ ($x = 0.2, 0.4, 0.6, 0.8$ or 1.0).

When comparing Fig. 9g and h with 9b and c, although the vibrational peaks of –N≡N– in Fig. 9g and h have disappeared or are not apparent, the stretching vibration peaks of the aromatic rings in the MO molecule at 1607 cm^{-1} are still quite strong, which shows that the –N≡N– bond in MO molecules is more susceptible to destruction than the aromatic ring during the electrochemical oxidation degradation process.

3.4. UV-vis spectrum analysis of MO reaction products degraded by the $La_{0.6}Nd_{0.4}FeO_3@AC$ composite electrode

Under the conditions of pH = 2.0 in MO wastewater, an electrolyte concentration of Na_2SO_4 of 7 g L^{-1} and an electrolytic current density of 400 mA dm^{-2}, the $La_{0.6}Nd_{0.4}FeO_3@AC$ composite electrode was used to catalyze the degradation of MO wastewater. After sampling every 2.5 minutes for each day, the

water samples were analyzed to produce a UV ultraviolet visible spectrum and the results are shown in Fig. 10.

The latest result shows that the maximum absorption wavelength of MO is affected by the initial pH.[37] When the initial pH is between 3.1–12.0, the maximum absorption wavelength $\lambda_{max} = 464$ nm, and moreover, $\lambda_{max} = 507$ nm for pH = 0.0–3.1.

As can be seen from Fig. 10a, when the pH of MO wastewater is 2.0, the maximum absorption wavelength (λ_{max}) position is basically consistent with 507 nm. Moreover, there are two distinct absorption peaks at 270 nm and 507 nm when the reaction time was 0 minutes. The former peak (270 nm) is in the ultraviolet band, which corresponds to $\pi \rightarrow \pi^*$ conversion of two adjacent aromatic rings in MO molecules. The latter peak (507 nm) is in the visible light band, which corresponds to the transition from $n \rightarrow \pi^*$ of the azo bond of the conjugated structure in MO molecules.[38] With an increase in reaction time (0–10 minutes), the intensity of the absorption peaks at 270 nm and 507 nm has been obviously weakened. At a reaction time of 7.5 minutes, the peak at 507 nm cannot be observed, and if the UV spectrum of MO wastewater at 7.5 minutes reaction time is magnified (Fig. 10b) only a weak absorption peak can be seen at 507 nm. However, in Fig. 10c, the peak at 507 nm has completely disappeared, and there is no new absorption peak, indicating that at 10 minutes reaction time, the MO in the wastewater has been completely degraded.

3.5. Gas chromatography-mass spectrometry (GC-MS) analysis on the electrocatalytic oxidation degradation of MO

For the purpose of determining the intermediates during the degradation process of methyl orange (MO), GC-MS was performed to study the qualitative composition of the intermediates. 20 mL MO wastewater (after degradation for 10 min) was extracted using dichloromethane (30 mL) for 30 min, then an amount of anhydrous sodium sulfate (Na_2SO_4) was added for dehydration and condensed to 5 mL by a rotary evaporator to satisfy the sampling conditions. The experimental results are shown in Fig. 11.

As can be seen from Fig. 11, the MO wastewater was degraded into a few intermediates during the degradation process, which indicated that the $La_{0.6}Nd_{0.4}FeO_3@AC$ composite anode shows excellent ability for the electrocatalytic degradation of MO. When the time was 3.13, 3.96, 4.05, 4.38, 4.47, 7.59 and 8.93 min, the intermediates are the aromatics and chain hydrocarbon species, which corresponds with the literature.[39,40] The results indicate that during the process of MO electrocatalytic degradation by a $La_{0.6}Nd_{0.4}FeO_3@AC$ composite anode, the large conjugated system formed by azo bonds and benzene rings in methyl orange molecules was destroyed. During the degradation process, at first, the azo bond will probably fracture to form benzene substances under the effect of the $La_{0.6}Nd_{0.4}FeO_3@AC$ composite electrocatalyst. With the electrocatalysis, the benzene ring will be further opened to form chain-like molecules, which are finally degraded to H_2O and CO_2. These results are consistent with the analysis of UV-vis and FT-IR spectra.
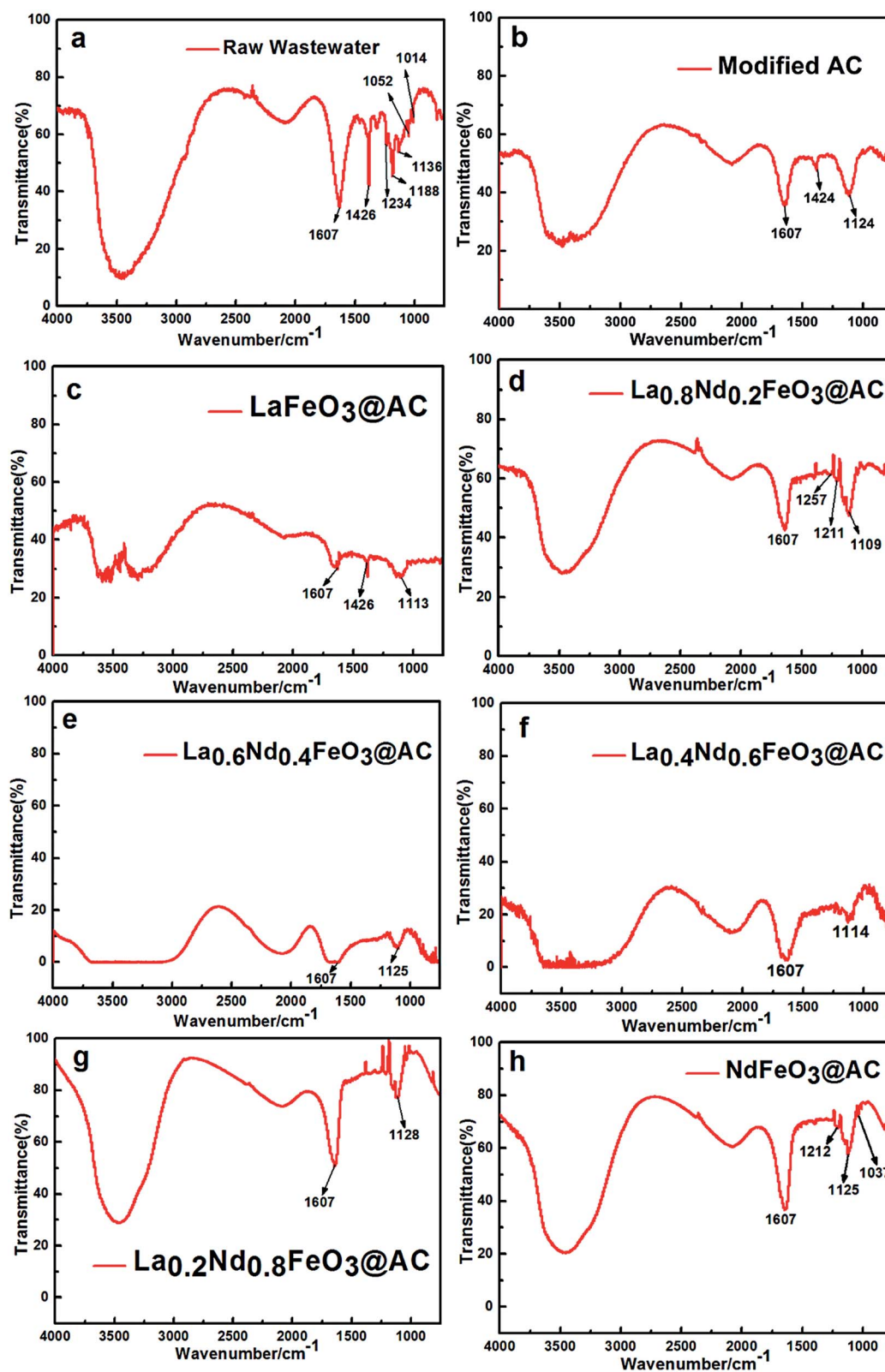
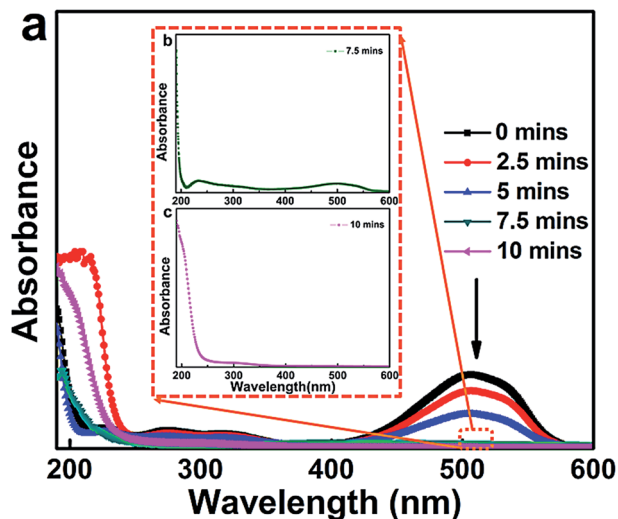Fig. 9   Fourier-transform infrared spectroscopy of MO using different composite anodes.

Fig. 10 UV-vis spectral changes of the 500 mg L^{-1} MO solution during the degradation process as a function of reaction time in the presence of 7 g L^{-1} Na$_2$SO$_4$, $I = 400$ mA dm^{-2} and pH = 2.0.
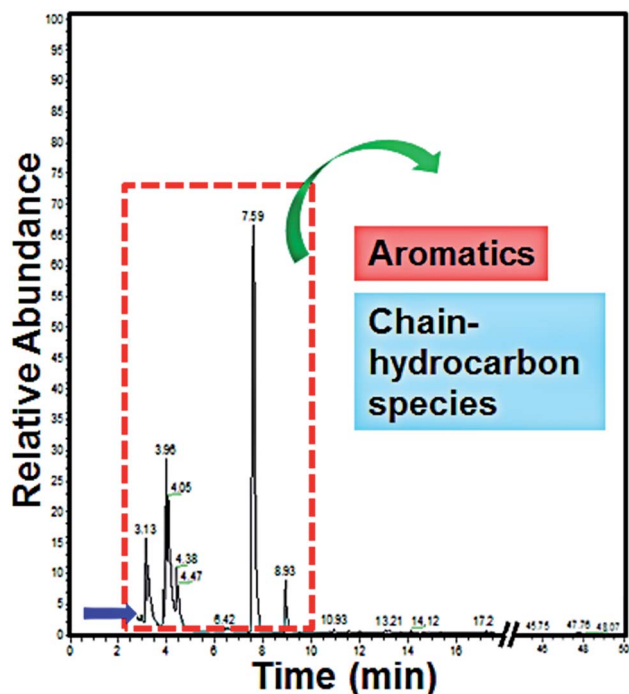

Fig. 11 GC-MS spectrum of MO wastewater after degradation by a La$_{0.6}$Nd$_{0.4}$FeO$_3$@AC composite anode for 10 min.

3.6.   Mechanism of electrocatalytic oxidation degradation of the La$_{0.6}$Nd$_{0.4}$FeO$_3$@AC composite anode

Fig. 12 shows the mechanism of a La$_{0.6}$Nd$_{0.4}$FeO$_3$@AC composite anode in the degradation of MO wastewater.

The main part is divided into a cathode oxygen reduction, a Fenton oxidation reaction system at the central part of the surface of the anode and the electrocatalytic oxidation of the MO reaction. Significantly, the segmentation process can probably be accounted for by a mechanism as follows:
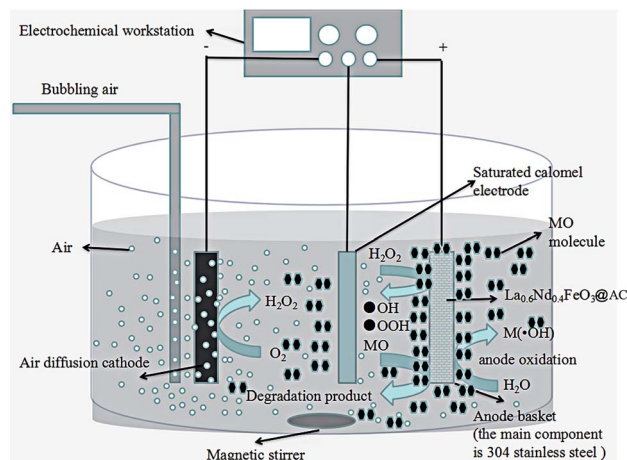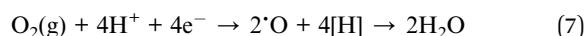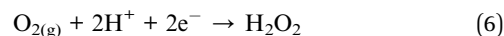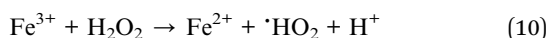

Fig. 12 Mechanism of MO degradation by a La$_{0.6}$Nd$_{0.4}$FeO$_3$@AC composite anode.

(I) Cathodic process – reduction of oxygen

$$O_{2(g)} + 2H^+ + 2e^- \rightarrow H_2O_2 \tag{6}$$

$$O_2(g) + 4H^+ + 4e^- \rightarrow 2{^\bullet}O + 4[H] \rightarrow 2H_2O \tag{7}$$

(II) Fenton oxidation reaction in the middle of the reaction system

(1) The iron wire supplied by the anode wire network migrates between the anode and cathode (middle), and the Fenton reaction occurs with the cathode H$_2$O$_2$
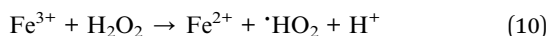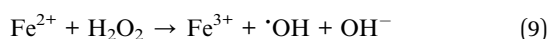
$$Fe - 2e^- \rightarrow Fe^{2+} \tag{8}$$

$$Fe^{2+} + H_2O_2 \rightarrow Fe^{3+} + {^\bullet}OH + OH^- \tag{9}$$

$$Fe^{3+} + H_2O_2 \rightarrow Fe^{2+} + {^\bullet}HO_2 + H^+ \tag{10}$$
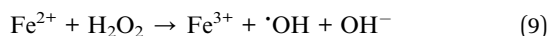
(2) Degradation process of MO in the middle of the electrode

$${^\bullet}OH + MO \rightarrow CO_2 + H_2O \tag{11}$$

$$HO_2{^\bullet} + MO \rightarrow CO_2 + H_2O \tag{12}$$
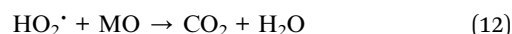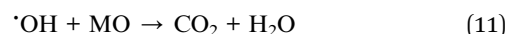
(III) Anode surface: the anode consists of two parts, the outer steel wire mesh anode and the composite catalyst (La$_{0.6}$Nd$_{0.4}$FeO$_3$@AC) anode inside the wire mesh. Their electrocatalytic oxidation process is as follows:

(1) Wire mesh near the anode

(i) The Fe^{2+} provided by the wire mesh reacts with the convective migration of H$_2$O$_2$ to the anode (or the electrochemical reaction of the anode) to produce a Fenton reaction
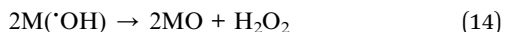
$$Fe - 2e^- \rightarrow Fe^{2+} \tag{8}$$

$$Fe^{2+} + H_2O_2 \rightarrow Fe^{3+} + {^\bullet}OH + OH^- \tag{9}$$

$$Fe^{3+} + H_2O_2 \rightarrow Fe^{2+} + {^\bullet}HO_2 + H^+ \tag{10}$$

(ii) The degradation process of MO

$$^\cdot OH + MO \rightarrow CO_2 + H_2O \quad (11)$$

$$HO_2^\cdot + MO \rightarrow CO_2 + H_2O \quad (12)$$
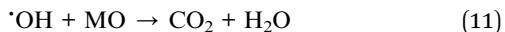
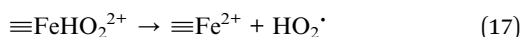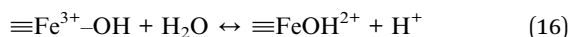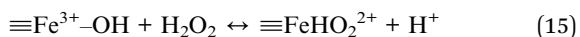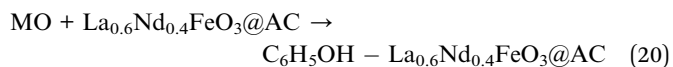(2) Electrochemical oxidation of H_2O on the surface of the $La_{0.6}Nd_{0.4}FeO_3$@AC composite catalyst anode and steel wire mesh

$$M + H_2O \rightarrow M(^\cdot OH) + H^+ + e^- \quad (13)$$
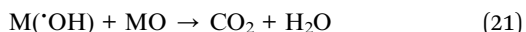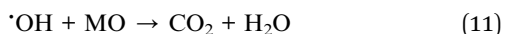
$$2M(^\cdot OH) \rightarrow 2MO + H_2O_2 \quad (14)$$

(3) Catalytic oxidation of reactive oxygen species on the anode surface of the composite catalyst ($La_{0.6}Nd_{0.4}FeO_3$@AC). ($\equiv Fe^{3+}$–OH means a fixed carrier above the oxide containing Fe^{3+})

$$\equiv Fe^{3+}\text{–OH} + H_2O_2 \leftrightarrow \equiv FeHO_2^{2+} + H^+ \quad (15)$$

$$\equiv Fe^{3+}\text{–OH} + H_2O \leftrightarrow \equiv FeOH^{2+} + H^+ \quad (16)$$

$$\equiv FeHO_2^{2+} \rightarrow \equiv Fe^{2+} + HO_2^\cdot \quad (17)$$

$$\equiv FeHO_2^{2+} + \equiv FeOH^{2+} \rightarrow 2\equiv Fe^{2+} + O_2 + H_2O \quad (18)$$

$$\equiv Fe^{2+} + H_2O_2 \rightarrow \equiv Fe^{3+}\text{–OH} + {}^\cdot OH + OH^- \quad (19)$$
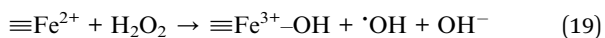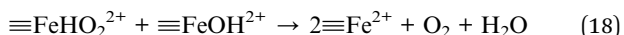
(4) Physical and electrochemical adsorption processes of MO on the $La_{0.6}Nd_{0.4}FeO_3$@AC anode surface of the composite catalysts

$$MO + La_{0.6}Nd_{0.4}FeO_3@AC \rightarrow$$
$$C_6H_5OH - La_{0.6}Nd_{0.4}FeO_3@AC \quad (20)$$

(5) MO degradation process on the anodic surface

$$^\cdot OH + MO \rightarrow CO_2 + H_2O \quad (11)$$

$$HO_2^\cdot + MO \rightarrow CO_2 + H_2O \quad (12)$$

$$M(^\cdot OH) + MO \rightarrow CO_2 + H_2O \quad (21)$$

4. Conclusions

In summary, we have prepared a series of perovskite-based composites, $La_{1-x}Nd_xFeO_3$@AC (x = 0, 0.2, 0.4, 0.6, 0.8 or 1.0), using a facile sol–gel method, and then the $La_{1-x}Nd_xFeO_3$–AC composite anodes were prepared for the electrochemical degradation of methyl orange (MO). In terms of the oxidative degradation of methyl orange, the $La_{0.6}Nd_{0.4}FeO_3$@AC composite anode has the strongest oxidation ability and stability, with MO wastewater and COD removal rates reaching 99.81% and 96.66% within 10 minutes, respectively. According to ultraviolet spectrum detection, the absorption peak of methyl orange wastewater at 507 nm has disappeared entirely, which indicated that MO has been thoroughly degraded. The results demonstrate that $La_{1-x}Nd_xFeO_3$@AC is a catalyst of unique significance with efficiency in the application of the treatment of MO. Furthermore, to the best of our knowledge, no research on the electrochemical properties of a $La_{1-x}Nd_xFeO_3$@AC composite material has been reported. Our studies in this current paper provide a series of novel perovskite–carbon composites, and ingenious methods for the electrochemical treatment of refractory pollutants, which are expected to play more important roles in the treatment of organic pollutant wastewater.

Author contributions

Q. J. W., S. Z., and H. R. W. conceived the idea and co-wrote the manuscript. Q. J. W., S. Z., F. F. W. and X. Z. Z. carried out the materials synthesis and the electrochemical catalysis. Q. J. W., S. X., S. Z. and J'e Q. performed the materials characterizations. H. R. W. proposed, planned and supervised the project. All of the authors discussed the results and commented on the manuscript. The manuscript was written through the contributions of all authors. All authors have given approval of the final version of the manuscript. Q. J. W. and S. Z. contributed equally to this work.

Conflicts of interest

The authors declare no conflict of interest.

Acknowledgements

References

1 M. A. Peña and J. L. G. Fierro, *Chem. Rev.*, 2001, **101**, 1981–2018.

2 S. Ponce, M. A. Peña and J. L. G. Fierro, *Appl. Catal., B*, 2000, **24**, 193–205.

3 V. A. Sadykov, L. A. Isupova, I. A. Zolotarskii, L. N. Bobrova, A. S. Noskov, V. N. Parmon, E. A. Brushtein, T. V. Telyatnikova, V. I. Chernyshev and V. V. Lunin, *Appl. Catal., A*, 2000, **204**, 59–87.

4 B. P. Barbero, J. A. Gamboa and L. E. Cadús, *Appl. Catal., B*, 2006, **65**, 21–30.

5 Y. Shimakawa, M. Azuma and N. Ichikawa, *Materials*, 2011, **4**, 153–168.

6 A. Cyza, A. Kopia, Ł. Cieniek and J. Kusinski, *Mater. Today: Proc.*, 2016, **3**, 2707–2712.

7 A. S. Nesaraj, S. Dheenadayalan and I. A. Raj, *J. Ceram. Process. Res.*, 2012, **13**, 601–607.

8 Y. Sun, X. Wu and L. Yuan, *Chem. Commun.*, 2017, **5**, 2499–2502.

9 O. P. Taran, A. B. Ayusheev and O. L. Ogorodnikova, *Appl. Catal., B*, 2016, **180**, 86–93.

10 P. Xiao, J. P. Hong, T. Wang, X. L. Xu, Y. H. Yuan, J. L. Li and J. J. Zhu, *Catal. Lett.*, 2013, **143**, 887–894.

11 S. D. Song, P. Zhang, M. F. Han and S. C. Singhal, *J. Membr. Sci.*, 2012, **415–416**, 654–662.

12 Y. X. Tong, Y. Zhang, B. Jiang, J. P. He, X. J. Zheng and Q. C. Liang, *IEEE Sens. J.*, 2017, **17**, 2404–2410.

13 M. Siemons, A. Leifert and U. Simon, *Adv. Funct. Mater.*, 2007, **17**, 2189–2197.

14 L. Y. Yang, S. Y. Lin, X. Yang, W. M. Fang and R. X. Zhou, *J. Hazard. Mater.*, 2014, **279**, 226–235.

15 H. He, H. X. Dai, L. H. Ng, K. W. Wong and C. T. Au, *J. Catal.*, 2002, **206**, 1–13.

16 P. Marco and C. Giacomo, *Chem. Rev.*, 2009, **109**, 6541–6569.

17 I. Sires, E. Brillas and M. A. Oturan, *Environ. Sci. Pollut. Res.*, 2014, **21**, 8336–8367.

18 N. Anglada, A. Urtiaga and I. Ortiz, *J. Chem. Technol. Biotechnol.*, 2009, **84**, 1747–1755.

19 E. Brillas, I. Sires and M. A. Oturan, *Chem. Rev.*, 2009, **109**, 6570–6601.

20 V. Kavitha and K. Palanivelu, *Water Res.*, 2005, **39**, 3062–3072.

21 S. A. Messele, F. Stüber, C. Bengoa, A. Fortuny, A. Fabregat and J. Font, *Procedia Eng.*, 2012, **42**, 1373–1377.

22 J. B. Xi, Q. J. Wang, J. Liu, L. Huan, Z. L. He, Y. Qiu, J. Zhang, C. Y. Tang, J. Xiao and S. Wang, *J. Catal.*, 2018, **359**, 233–241.

23 J. B. Xi, H. Y. Sun, D. Wang, Z. Y. Zhang, X. M. Duan, J. W. Xiao, F. Xiao, L. M. Liu and S. Wang, *Appl. Catal., B*, 2018, **225**, 291–297.

24 S. A. Messele, O. S. G. P. Soaresb, J. J. M. Órfãb, F. Stüber, C. Bengoa, A. Fortuny, A. Fabregat and J. Font, *Appl. Catal., B*, 2014, **154–155**, 329–338.

25 S. D. Li and X. L. Wang, *Optik*, 2015, **126**, 408–410.

26 W. H. Bragg and W. L. Bragg, *Proc. R. Soc. London, Ser. A*, 1913, **88**, 428–438.

27 M. Yousefi, S. S. Zeid and M. K. Motlagh, *Current Chemistry Letters*, 2017, **6**, 23–30.

28 O. M. Hemeda, M. M. Barakat and D. M. Hemeda, *Turk. J. Phys.*, 2003, **27**, 537–549.

29 X. F. Tang, Y. G. Li, X. M. Huang, Y. D. Xu, H. Q. Zhu, J. G. Wang and W. J. Shen, *Appl. Catal., B*, 2006, **62**, 265–273.

30 Y. Zheng, K. Z. Li, H. Wang, D. Tian, Y. H. Wang, X. Zhu, Y. G. Wei, M. Zheng and Y. M. Luo, *Appl. Catal., B*, 2017, **202**, 51–63.

31 B. Lai, Y. X. Zhou, Y. Ping, J. H. Yang and J. L. Wang, *Chemosphere*, 2013, **90**, 1470–1477.

32 T. D. Nguyen, N. H. Phan, M. H. Do and K. T. Ngo, *J. Hazard. Mater.*, 2011, **185**, 653–661.

33 S. S. Lin, C. L. Chen, D. J. Chang and C. C. Chen, *Water Res.*, 2002, **36**, 3009–3014.

34 H. Chen, A. Sayari and A. Adnot, *Appl. Catal., B*, 2001, **32**, 195–204.

35 W. Yao, S. J. Yu, J. Wang, Y. D. Zou, S. S. Lu, Y. J. Ai, N. S. Alharbi, A. Alsaedi, T. Hayat and X. K. Wang, *Chem. Eng. J.*, 2017, **307**, 476–486.

36 Y. Liu and D. Z. Sun, *Appl. Catal., B*, 2007, **72**, 205–211.

37 E. W. Wang, S. M. Lei, S. C. Zhang, T. Huang and L. L. Zhong, *J. Wuhan Univ. Technol., Mater. Sci. Ed.*, 2015, **30**, 185–192.

38 J. Fan, Y. H. Guo, J. J. Wang and M. H. Fan, *J. Hazard. Mater.*, 2009, **166**, 904–910.

39 S. M. Robert, F. X. Webster and D. J. Kieml, *Spectrometric identification of organic compounds*, East China University of Science And Technology Press, ShangHai, 2007, pp. 85–127.

40 W. Zhong, T. Jiang, Y. L Dang, J. K. He, S. Y. Chen, C. H. Kuo, D. Kriz, Y. T. Meng, A. G. Meguerdichiana and S. L. Sui, *Appl. Catal., A*, 2018, **549**, 302–309.